CrossMark

ORIGINAL

Numerical investigation of turbulent flow within a channel with chamfered edge ribs in stream-wise direction

Vincenzo Bianco[1] · Walter Borreani[1,2,3] · Guglielmo Lomonaco[1,3]

Abstract The present paper reports a numerical investigation of a forced convection water flow within a two-dimensional ribbed channel. A uniform heat flux is applied on the external walls. The flow regime is turbulent and Reynolds numbers are in the range $10 \cdot 10^3 \div 100 \cdot 10^3$. Square and chamfered rib shapes with different arrangements are analyzed in terms of various dimensionless heights and pitches of elements. The investigation is accomplished by using a CFD code and its aim consists in finding of arrangements to obtain a high Performance Evaluation Criterion (PEC). Results are presented in terms of temperature and velocity fields, profiles of average Nusselt number, average heat transfer coefficients and required pumping power. Heat transfer enhancement increases with the ribs presence, but it is accompanied by an increasing pumping power. In particular, the best performances in terms of Nusselt are shown for $p/e = 4$ and 12 for both the square and chamfered cases. The heat transfer improves as Reynolds number raises, but a substantial increase of pumping power is also observed. The utilization of chamfered ribs allows to increase the PEC, especially at low Re. The maximum PEC is equal to 1.3 and it is obtained for $Re = 10^4$ and $p/e = 4$.

✉ Vincenzo Bianco
   vincenzo.bianco@unige.it

1   DIME/TEC, Division of Thermal Energy and Environmental
    Conditioning, University of Genoa, Via All'Opera Pia 15/A,
    16145 Genoa, Italy

2   Ansaldo Nucleare S.p.A, Corso F.M. Perrone 25, 16152 Genoa, Italy

3   INFN, Via Dodecaneso 33, 16146 Genoa, Italy

Nomenclature

a	thermal diffusivity, m²/s
cp	specific heat, J/kg K
d	diameter, m
e	rib height, m
f	friction coefficient Eq. (10)
H	channel height, m
L	length, m
k	turbulent kinetic energy, m²/s²
Nu	Nusselt number Eq. (9)
p	rib pitch, m
P	pressure, Pa
PEC	performance evaluation criteria index Eq. (11)
PP	pumping power, W
Pr	Prandtl number
q	heat flux, W/m²
Re	Reynolds number Eq. (8)
s	channel thickness, m
T	temperature, K
T*	dimensionless temperature, $T^* = T/T_{bulk}$
u	velocity component, m/s
W	channel width, m
w	rib width, m
x, y	spatial coordinates, m

Greek symbols

δ	Kronecher delta function
λ	thermal conductivity, W/mK
μ	dynamic viscosity, Pa s
ν	kinematic viscosity, m²/s
ρ	density, kg/m³
σ	turbulent Prandtl number
τ	wall shear stress, kg/m²
ω	rate of dissipated turbulent kinetic energy

Subscripts

a	ambient
avg	average
f	fluid
in	inlet section
m	mass
out	outlet section
s	smooth
T	turbulent
w	wall

1 Introduction

The study of methodologies to enhance heat transfer represents a topic of relevant interest for many researchers engaged in the study of heat exchange systems. This interest has been emphasized in the last years due to the size reduction of components and stricter temperature limitations of thermal systems.

To this scope, different options are available. For example, by installing fins it is possible to increase the heat transfer area by achieving higher heat flows, or the heat exchange fluid can be substituted with a more effective one in order to enhance the heat transfer, as might be the case of nanofluids [1].

Another ingenious way to increase the heat transfer coefficient is to install small ribs on the walls of a channel, so that the mixing level of cooler and warmer fluids is increased. The boundary layer near the walls is interrupted by the presence of ribs (flow separation) and this avoid its development. As known from basic heat transfer, the average value of heat transfer coefficient in the development phase is higher than that in the fully developed zone. Therefore, if the flow never reaches the fully developed condition, a higher heat transfer coefficient is detected.

It is to be mentioned that the enhancement of heat transfer by flow separation and reattachment caused by ribs is significantly higher compared to that achieved by the increased heat transfer area due to the fin effect of the ribs [2].

On the other hand, the installation of ribs introduces obstacles to the flow, hence the friction factor increases as well as the pumping power. For this reason, it is necessary to optimize shape, dimensions and position of the ribs.

Rib-roughened walls are extensively applied for heat transfer augmentation in different devices and have been largely investigated by many researchers by developing both numerical and experimental investigations.

Tanda [3] proposed an experimental investigation to determine the distribution of the heat transfer coefficient in channels with ribs turbulators. He tested rectangular, squared and V-shaped ribs and determined the increase of heat transfer coefficient with respect to smoothed channels. Likewise,

Promvonge and Thianpong [4] conducted experiments to assess turbulent forced convection heat transfer and friction loss behaviors for air flow through a constant heat flux channel fitted with different shaped ribs. They considered triangular (isosceles), wedge (right-triangular) and rectangular shapes ribs. They concluded that the wedge ribs pointing downstream offer the highest heat transfer performances, but also the largest increase in friction factor. The same research group also proposed an experimental analysis of the effects of combined ribs and winglet type vortex generators on forced convection heat transfer and friction loss behaviors for turbulent airflow through a constant heat flux channel [5]. They investigated different arrangements and detected the most convenient solution.

When it is considered the utilization of ribs, there is the necessity to understand which is the optimal configuration to adopt. To this aim Kim and Kim [6] proposed a numerical procedure to optimize the shape of a two-dimensional channel with periodic ribs mounted on both the walls to enhance turbulent heat transfer. According to their procedure, they obtained the optimal channel shape, pitch-to-rib height ratio and distance between opposite ribs. By employing a similar approach, Kim et al. [7] obtained the best rib geometry based on three design variables, namely rib height, rib width, and rib pitch. Xie et al. [8] employed square cross-section ribbed channels with different arrangements of downstream half-size ribs to determine the most optimal configurations for augmenting heat transfer rates with minimized pressure drop penalties. They numerically analyzed six ribbed channels and the results revealed that the usage of downstream ribs is a suitable way to decrease the pressure loss and improve the flow structure, while keeping comparable enhancement in heat transfer.

Other authors performed numerical simulations of ribbed channels in order to understand which is the best approach to follow. Viswanathan and Tafti [9] proposed a numerical investigation of a hydrodynamic and thermally developed turbulent flow for a stationary duct with square ribs aligned normal to the main flow direction. They tested different turbulence models and concluded that the DES model represents the best compromise in terms of results accuracy and simulation time. Instead, Labbè [10] proposed the utilization of LES turbulence model to simulate the thermal and velocity fields in a ribbed channel. He attempted to simulate a small section of the channel with one rib cell and applied a periodic boundary condition on the streamwise direction. The results resulted to be very close to the experimental measurements. Similarly, Dritselis [11] tested LES model to simulate velocity and temperature fields within a ribbed channels. He analyzed different subgrid-scale turbulence models and concluded that all the considered models are able to reproduce the relevant physics associated with ribbed channels.

Ribbed surfaces have been proposed in a number of applications when there is the necessity to increase the heat transfer

rate. Tan et al. [12] utilized a ribbed surface impinged by air jets and observed an increase of heat transfer rate in various configurations up to 30%. Similarly, Caliskan and Baskaya [13] performed an experimental investigation of impinging jets investing surfaces with V-shaped and convergent-divergent ribs. They detected an increase of the heat transfer rate from 4% to 27% with respect to the smooth plate. Yadav and Bhagoria [14], Karwa et al. [29] and Layek et al. [30], applied trapezoidal shaped ribbed surfaces to increase the heat transfer in a solar heater. They optimized roughness and flow parameters of the solar air heater by considering a thermo-hydraulic performance parameter based on constant pumping power requirements.

The aim of the present paper is to propose a new shape for ribs, namely a square rib with chamfered corner in the stream-wise direction, in order to decrease pressure losses, while maintaining substantially unchanged the heat transfer enhancement within a channel composed by two parallel plates. To the best of authors' knowledge it is the first time that such kind of ribs have been proposed and analyzed in a wide range of turbulent Re numbers. A numerical simulation is performed by using the commercial CFD software Ansys-Fluent to analyze five different values of the distance among the ribs and Re number ranging from $10 \cdot 10^3$ up to $100 \cdot 10^3$.

The detailed characteristics in terms of velocity and temperature fields, as well as the Performance Evaluation Criterion (PEC) are analyzed and discussed in order to understand the possible benefits deriving by chamfering the corner in the flow direction.

2 Model

2.1 Mathematical model

A computational fluid-dynamic analysis of a two-dimensional channel model, as shown in Fig. 1, is considered in order to evaluate its thermal and fluid-dynamic behaviors for different Reynolds numbers and ribs pitch.

The channel is composed by two aluminum parallel plates placed at a distance of 20 mm. The plates have a thickness of 3 mm, length of 250 mm and infinite width, with a constant uniform heat flux applied on the external channel walls. Different inlet velocities are considered in the range of turbulent regime and the working fluid is water with constant properties.

Five geometrical configurations are investigated: smooth channel (Fig. 1a) and ribbed channel with pitch "p" 4, 8, 12 and 16 (Fig. 1b). The ribs shape are square and square with a chamfered corner, with height "e" and width "w" equal to 1 mm.

A numerical analysis is developed by using the CFD solver Ansys Fluent 14.0 in conjunction with Ansys ICEM CFD Hexa Block meshing tool.

The governing equations of continuity, momentum and energy are solved for a turbulent flow in rectangular coordinates under the hypotheses of steady-state, two-dimensional, incompressible, constant properties flow conditions with conjugate heat transfer, according to the following equations [28]:

Continuity:

$$\frac{\partial u_x}{\partial x} + \frac{\partial u_y}{\partial y} = 0 \tag{1}$$

Momentum:

x direction:

$$\frac{\partial(u_x u_x)}{\partial x} + \frac{\partial(u_y u_x)}{\partial y} =$$
$$= -\frac{1}{\rho}\frac{\partial p}{\partial x} + \frac{\partial}{\partial x}\left[(\nu + \nu_T)\frac{\partial u_x}{\partial x}\right] + \frac{\partial}{\partial y}\left[(\nu + \nu_T)\frac{\partial u_x}{\partial y}\right] + \frac{\partial}{\partial x}\left[(\nu + \nu_T)\frac{\partial u_x}{\partial x}\right]$$
$$+ \frac{\partial}{\partial y}\left[(\nu + \nu_T)\frac{\partial u_y}{\partial x}\right] \tag{2}$$

y direction:

$$\frac{\partial(u_x u_y)}{\partial x} + \frac{\partial(u_y u_y)}{\partial y} =$$
$$= -\frac{1}{\rho}\frac{\partial p}{\partial y} + \frac{\partial}{\partial x}\left[(\nu + \nu_T)\frac{\partial u_y}{\partial x}\right] + \frac{\partial}{\partial y}\left[(\nu + \nu_T)\frac{\partial u_y}{\partial y}\right] + \frac{\partial}{\partial x}\left[(\nu + \nu_T)\frac{\partial u_x}{\partial y}\right]$$
$$+ \frac{\partial}{\partial y}\left[(\nu + \nu_T)\frac{\partial u_y}{\partial y}\right] \tag{3}$$

Energy:

$$\frac{\partial(u_x T)}{\partial x} + \frac{\partial(u_y T)}{\partial y} = \frac{\partial}{\partial x}\left[\left(\frac{\nu}{Pr} + \frac{\nu_T}{Pr_T}\right)\frac{\partial T}{\partial x}\right]$$
$$+ \frac{\partial}{\partial y}\left[\left(\frac{\nu}{Pr} + \frac{\nu_T}{Pr_T}\right)\frac{\partial T}{\partial y}\right] \tag{4}$$

The turbulence model adopted in this analysis is the Shear-Stress Transport (SST) k-ω, reported below in the form originally developed by Menter [23] and implemented in Ansys Fluent 14.0 in steady-state form:

$$\frac{\partial}{\partial x_i}(\rho k u_i) = \frac{\partial}{\partial x_j}\left(\Gamma_k \frac{\partial k}{\partial x_j}\right) + \tilde{G}_k - Y_k + S_k \tag{5}$$

$$\frac{\partial}{\partial x_i}(\rho \omega k u_i) = \frac{\partial}{\partial x_j}\left(\Gamma_\omega \frac{\partial \omega}{\partial x_j}\right) + G_\omega - Y_\omega + D_\omega + S_\omega \tag{6}$$

where G_k is the production of turbulence kinetic energy due to mean velocity gradients, G_ω represents the generation of ω, Γ_k and Γ_ω respectively represent the effective diffusivity of k

Fig. 1 Schematic of the geometrical conjugated thermal-fluid model: (**a**) smooth channel, (**b**) ribbed channel, (**c**) ribbed channel detail and ribs shape. All the dimensions are in mm
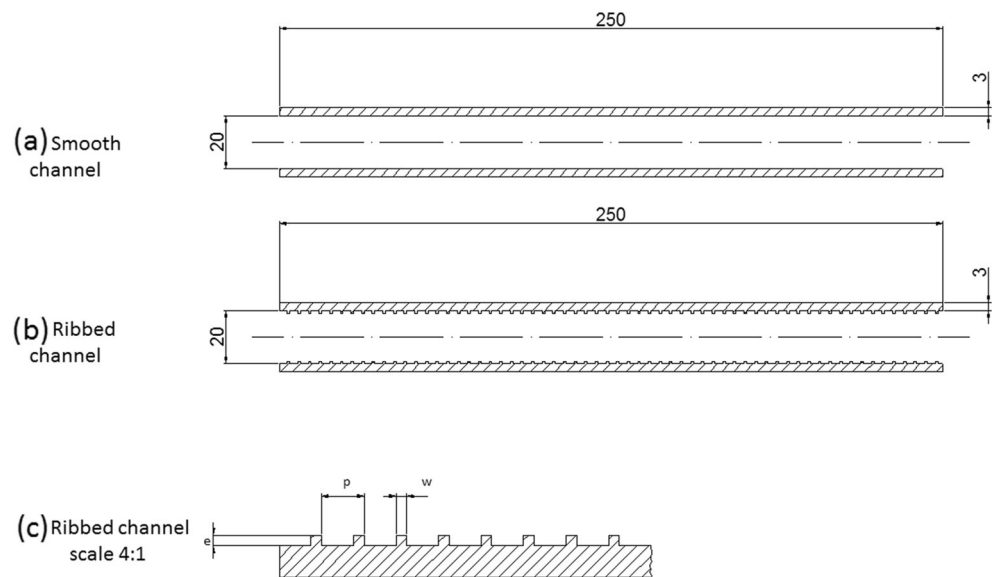
and ω due to the turbulence, D_ω is the cross-diffusion term and S_k and S_ω are user-defined source terms (not implemented in this case); for the calculations details see [24–26].

Moreover, a two dimensional conduction model is employed in the heated walls and the equation for the steady-state regime is:

$$\frac{\partial}{\partial x_i}\left(\lambda \frac{\partial T}{\partial x_i}\right) = 0 \tag{7}$$

The scheme adopted for interpolation is a second-order upwind for all the discretized equations, namely the Green-Gauss Node-based Gradients method. Finally, a coupled pressure-based solver is utilized in order to obtain a faster convergence with respect to the segregated SIMPLE/ SIMPLEC and PISO scheme [27].

The assigned boundary conditions, schematized in Fig. 2, are the following:

– inlet section: uniform velocity, dependent on the considered Reynolds number, and temperature profile, set at 300 K;
– outlet section: pressure outlet conditions with relative pressure set at 0 Pa;

– external wall surface: uniform surface heat flux, equal to 20 kW/m² for all simulations.

On wall-fluid interface, a non-slip velocity condition and a coupled heat transfer, with creation of the shadow surface for the conjugate heat transfer problem calculations [27], are imposed.

The physical properties of the working fluid and solid walls are determined at 300 K.

Calculations have been performed without any developed velocity and temperature profile at the inlet of the channel, because the particular geometry and the hypothesis of turbulent flow, with the consequent formation of a quasi-flat input profile, has no advantage in terms of convergence and do not significantly improve the accuracy of the results. The flow through the ribbed channel experienced anyway a development phase.

2.2 Geometrical model and data reduction

The channel has square ribs on the walls (Fig. 1b-c) and, in analogy with the analysis performed in [15], the roughness parameters are determined by rib height (e), pitch (p), width (w) and shape of turbulators. These parameters have been

Fig. 2 Sketch of the boundary conditions

expressed as dimensionless roughness parameters: relative pitch, p/e, relative height, e/d, and relative width, w/e.

In this work, only the shape of the turbulators and the pitch was changed and all the calculations are conducted for e/d = 0.05 and w/e = 1.

The considered dimensionless parameters are the Reynolds number (eq. 8), the average Nusselt number (eq. 9), the friction factor (eq. 10) and the PEC index (eq. 11), expressed by the following relations:

$$Re = \frac{\rho u_{inlet} d_h}{\mu} \tag{8}$$

$$Nu_{av} = \frac{q' d_h}{\lambda \left(T_{avg,wall} - T_{bulk}\right)} \tag{9}$$

where $(T_{avg,wall} - T_{bulk})$ is the difference between the average wall temperature and the average fluid bulk temperature.

$$f = 2\Delta P \frac{d_h}{L} \frac{1}{\rho u_{avg}^2} \tag{10}$$

The PEC index is introduced in order to compare the thermal performance with respect to the pressure drop [15, 28]:

$$PEC = \frac{\left(Nu_{avg}/Nu_{avg,s}\right)}{\left(f/f_s\right)^{1/3}} \tag{11}$$

The two-dimensional channel, depicted in Fig. 1, has a length, L, equal to 250 mm, the hydraulic diameter, d_h, is equal to 20.0 mm and the thickness of the wall, in aluminum, is equal to 3 mm.

The range of dimensionless roughness parameters and Reynolds numbers employed in this investigation are given below:

–　　Reynolds number, Re, from $10 \cdot 10^3$ to $100 \cdot 10^3$;
–　　Relative roughness pitch (p/e) from 4 to 16 with a step equal to 4;
–　　Shape of ribs: square and square with chamfer (Fig. 3).

The chamfered ribs (Fig. 3) are expected to provoke a lower pressure drop and, consequently, a reduction in the required Pumping Power (PP), defined as

$$PP = \dot{V}\Delta P [W] \tag{12}$$

The chamfered geometry is implemented for its constructive simplicity, in terms of mechanical manufacturing. For example, the processing technology required to implement a rounded edge instead of the chamfered is much more complicated and expensive.

2.3 Computational grid sensitivity analysis and results validation

In order to perform the grid independence analysis to avoid possible errors depending on the mesh resolution, four different grids in terms of number of elements are tested on the channel with square ribs, p/e = 8, for Re = $50 \cdot 10^3$ and water as working fluid. The grids have about 1, 2, 4 and 8 million of nodes, respectively. Moreover, on the basis of previous literature [29, 30], two turbulent models, namely k-ω SST and k-ε RNG, are taken into account and compared.

The grid is fully structured in all the cases and configured to achieve an y⁺ value lower than 1 for all of them. In fact, taking as reference the worst case, i.e. Re in the order of $1 \cdot 10^4$, the required wall distance for the first node near the wall, computed as reported in [31], is about $3.5 \cdot 10^{-6}$ m and the proposed grid satisfies this requirement.

Tables 1 and 2 show how with both turbulence models, by considering the low percentage deviation and the computational cost required, the 2 million nodes grid results the better choice. On the other hand from the point of view of the turbulence model, there is a considerable difference in terms of pressure drop prediction, as shown in Table 3.

As reported in [32–34], in order to predict accurately pressure drop, heat transfer coefficient and reattachment length, the suggested turbulence model is k-ω SST, and

Fig. 3 Comparisons between the two different ribs: (**a**) square ribs geometry, (**b**) chamfered ribs geometry. All the dimensions are in mm
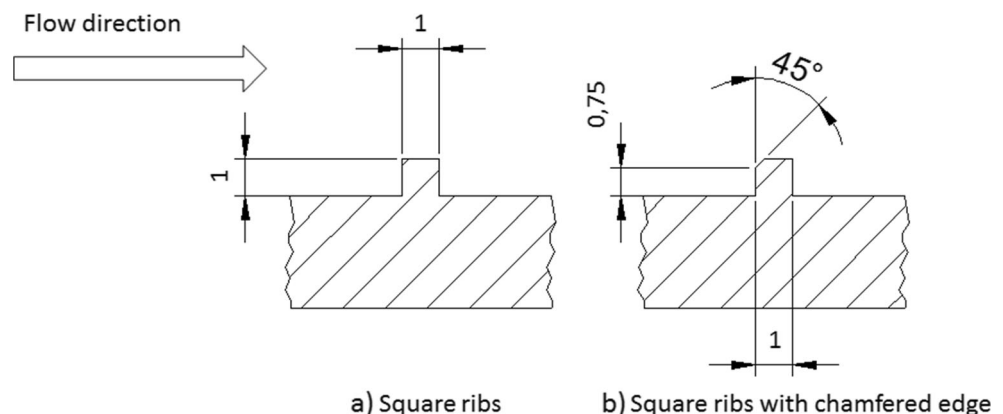
Table 1 k-ω SST grid sensitivity analysis (p/e = 8, Re = 50·10³)

Grid size [Mnodes]	ΔNu_{avg}	Δf
1	-	-
2	6.1%	0.1%
4	1.6%	1.4%
8	1.2%	0.1%

Table 3 Turbulence model sensitivity analysis (p/e = 8, Re = 50·10³)

Turbulence model	Nu_{avg}	f
k-ω SST	406.0	8.3·10⁻²
k-ε RNG	432.0	10.4·10⁻²
% diff.	1.3%	25.5%

for this reason it has been used for the simulations performed in this work.

The selected fully structured grid has been built by means of the Hexa blocking module of Ansys ICEM 14.0. It is configured with multiple interconnected volumes, in particular for the ribs, chamfer, wall and fluid volume, so that it can be selected if they are fluid or solid zones (Fig. 4). Physical properties of fluid and solid zones are reported in Table 4.

With this mesh configuration, it is possible to perform all the simulations by using the same grid, selecting the appropriate conditions for the zones, as reported in Table 5. In this way, problems related to different nodes configurations or wall treatment behavior are avoided.

A steady-state solution and a coupled solver are considered to solve the governing equations, linearized implicitly with respect to dependent variables. A second-order upwind scheme for energy, momentum, turbulent kinetic energy and rate of dissipated turbulent kinetic energy equations is selected. The incoming flow is assumed turbulent with a turbulence intensity of 1% and at ambient temperature and pressure.

To check the convergence of the solution the residuals of mass, momentum, energy and turbulence equations are monitored. Moreover, also the stabilization of the trend of pressure drop and wall temperature within the channel are monitored.

Numerical results are validated by comparing with data obtained from correlations available in literature in terms of average Nusselt number and friction coefficient for a smooth channel. The following correlations are adopted for water flow:

– Dittus-Boelter correlation [16]:

$$Nu_{avg,s} = 0.024 \, \mathrm{Re}^{0.8} Pr^{0.4},$$

valid for $0.5 < Pr < 120$, $6.0·10^3 < \mathrm{Re} < 1.0·10^7$, $(L/d_h) > 60$

Table 2 k-ε RNG grid sensitivity analysis (p/e = 8, Re = 50·10³)

Grid size [Mnodes]	ΔNu_{avg}	Δf
1		
2	1.3%	0.1%
4	2.8%	0.8%
8	1.1%	0.6%

– Petukhov correaltions [17]:

$$Nu_{avg,s} = \frac{\mathrm{RePr}(f/8)}{1.07 + 12.7(f/8)^{1/2}\left(Pr^{2/3}-1\right)}$$

with $f_s = (1.84 \log_{10} \mathrm{Re} - 1.64)^{-2.}$

valid for $0.5 < Pr < 200$, $1.0·10^4 < \mathrm{Re} < 5.0·10^6$

– Gnielinsky correlation [18]:

$$Nu_{avg,s} = \frac{(\mathrm{Re}-1000)\mathrm{Pr}\left(f/8\right)}{1 + 12.7\left(f/8\right)^{1/2}\left(Pr^{2/3}-1\right)}$$

with $f_s = (0.79 \ln \mathrm{Re} - 1.64)^{-2}$

valid for $0.5 < Pr < 160$, $2300 < \mathrm{Re} < 5.0·10^6$

Fig. 5(a) shows the comparison between the correlations and the numerically calculated Nusselt numbers. It can be noticed a good agreement among the CFD values and the correlations. CFD results are similar at the:

– Dittus-Boelter correlations in the interval $10·10^3 < \mathrm{Re} < 40·10^3$;
– Petukhov correlation inside the interval $50·10^3 < \mathrm{Re} < 70·10^3$;
– Gnielinsky correlations inside the interval $80·10^3 < \mathrm{Re} < 100·10^3$;

Numerical results highlight a good agreement with the proposed correlations, both in terms of Nusselt and friction factor (Fig. 5a-b), therefore it can be said that the proposed approach is appropriate. Furthermore, a validation of the calculations for the ribbed channel is also proposed. Comparisons with the data provided in [15] are reported in terms of Nu ratio (e.g. the ration between the Nu of the ribbed channel and that of the smooth channel). The same geometry and flow conditions as in [15] are considered and the results are in good agreement, as shown by Fig. 5(c).

In light of this, it can be concluded that the proposed numerical model is applicable to simulate ribbed channels with a satisfactory accuracy.

Fig. 4 Overview of the computational grid: (**a**) zone layout and (**b**) layering between solid and fluid zone
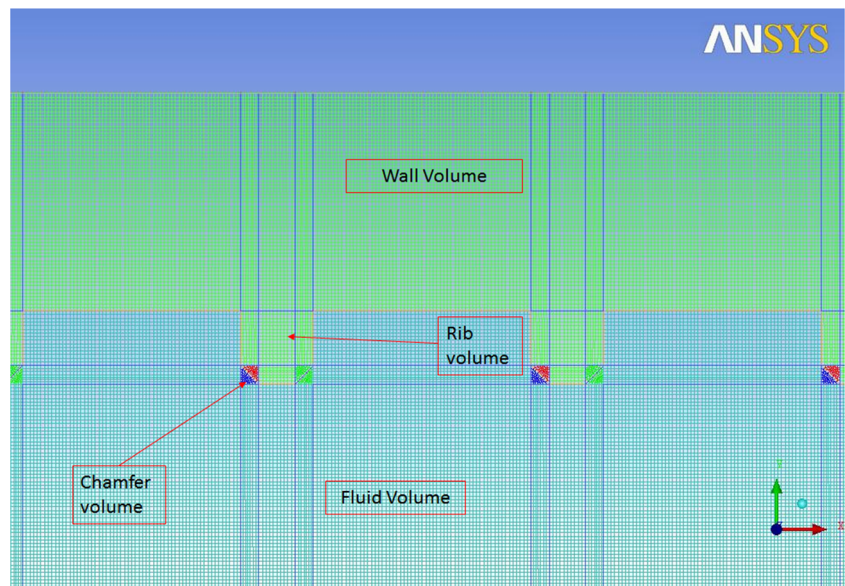
3 Results and discussion

Results are reported in terms of average Nusselt number ratio (ribbed vs. smooth channel), pressure drop and required pumping power profiles as a function of Reynolds number and dimensionless roughness parameter. The results are presented at first by the point of view of ribbed channel with and without chamfer and then by comparing the performance according to the detected values of the PEC index.

Fig. 6(a) reports the average Nusselt number ratio for squared and chamfered ribs. The ratio shows that the thermal performance increases in both the cases and it is higher at low Reynolds, whereas at higher Re the Nu ratio tends to decrease. This is due to the fact that at higher Re the motion is, independently from the presence of ribs, very turbulent; therefore the additional effect of the ribs is more limited with respect to the low Re cases.

The Nu ratio also varies according to the p/e ratio, in particular it decreases as p/e increases. This is due to the fact that for high p/e there is a more extensive re-attachment of the flow, as it will be shown in the following. This will reduce the turbulence intensity and, consequently, the Nusselt number. Therefore, it can be said that as Re and p/e increases the impact of ribs is heavily reduced.

The thermal performance is slightly influenced by the chamfer in the flow impingement direction. At high Reynolds number there are practically the same values of Nu ratio for squared and chamfered ribs, whereas at low Re some differences are highlighted.

For p/e = 4, 8, 12 and $10 \cdot 10^3 \leq Re \leq 40 \cdot 10^3$, the ratio shows the following trend: the chamfered edge case presents higher values of the Nu ratio, but at $Re = 30 \cdot 10^3$ it becomes lower in all the three cases, and returns to be almost the same at $Re = 40 \cdot 10^3$. The same instability phenomenon persists at $Re = 60 \cdot 10^3$.

Generally, the presence of the chamfer is negligible in terms of heat exchange performance. This is due to the fact that it does not influence the global turbulence intensity within the channel. On the contrary, there is a substantial local effect in terms of energy dissipation, because the chamfered corner introduces an energy loss which is much lower with respect to a 90° corner, as shown in Fig. 6(b).

The effect of chamfer corners is very significant at high Re in terms of reduction of pressure losses, because the high velocity plays a substantial role in the vortex flow detachment, as reported in the following where stream functions are discussed. For p/e = 16, the chamfer causes a significant decrease of the pressure drop with respect to the square ribs configuration, with values lower than 25% for Re greater than $70 \cdot 10^3$.

Table 4 fluid properties evaluated at 300 K

	ρ [kg/m^3]	μ [Pa·s]	λ [W/m K]	c_p [J/kg K]
Water	998	998E-06	0.597	4182
Aluminum	2719	-	202.4	871

Table 5 mesh configurations for different considered cases

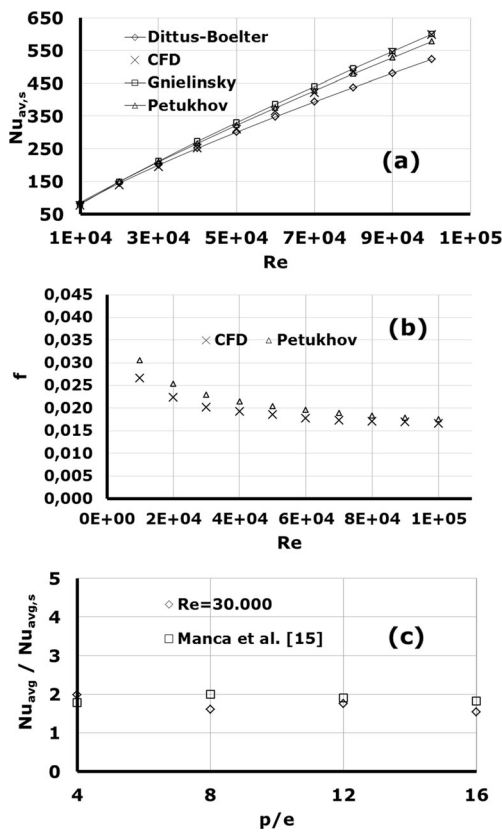| ZONES	Smooth channel	Ribbed channel	Ribbed channel with chamfer
Wall	Solid	solid	solid
Fluid	Fluid	fluid	fluid
Rib	Fluid	solid	solid
Chamfer	Fluid	solid	solid

Fig. 5 Validation of the numerical results: (a) numerical Nu vs. analytical correlations, (b) numerical friction factor vs. analytical correlations, (c) ribbed channel at Re = 30·10³ compared to the results presented in [22]

previously exposed, the influence of the chamfer related to the Nusselt number is negligible.

The profile of the average Nusselt number ratio, reported in Fig. 6(c), highlights that the trend at different p/e values is not monotonic. There is a maximum value for p/e = 4, then an oscillating behavior is detected, with a relative maximum for p/e = 12. This oscillating behavior can be explained with the fact that according to the p/e ratio, the interaction between the fluid flow and the ribbed surfaces is largely affected. In fact, at p/e = 4 the gap between two ribs has the minimum dimension, this allows the formation of small and unstable vortex structures that tend to break up and new fluid is recalled from outside the gap, Fig.7(a), by determining a high Nu value.

When p/e increases to the value of 8, it happens that larger vortex structures can originate and, as shown in Fig. 7(b), they tend to recirculate by worsening the heat exchange, in fact Nu values are lower. Furthermore, for p/e = 12, Fig. 7(c) shows that the vortex structure does not fill the gap completely and a re-attachment of the flow is detected. This reduces the recirculation effect detected at p/e = 8 allowing a better heat exchange by recalling fluid from the main stream. Finally at p/e = 16, Fig. 7(d), the re-attachment surface is more extended, but the number of ribs present in the channel is substantially lower with respect to p/e = 12, therefore the effect is more limited, resulting in a lower Nu value. The illustrated mechanisms justify the oscillating trend detected in Fig. 6(c), which can be summarized as follows:

– p/e = 4: creation of unstable vortexes which break up and recall fluid from the main stream;
– p/e = 8: creation of a stable vortex which recirculates and determines a worsening of the heat exchange;

Figs. 6(c) and (d) show the average Nusselt number ratio and the required pumping power profiles at constant Reynolds number for different values of relative roughness, p/e. As

Fig. 6 Numerical results for square and chamfered ribs: (a) average Nu ratio profile as function of Re, (b) pressure losses as function of Re, (c) average Nu ratio profile for different pitches, (d) required pumping power for different pitches
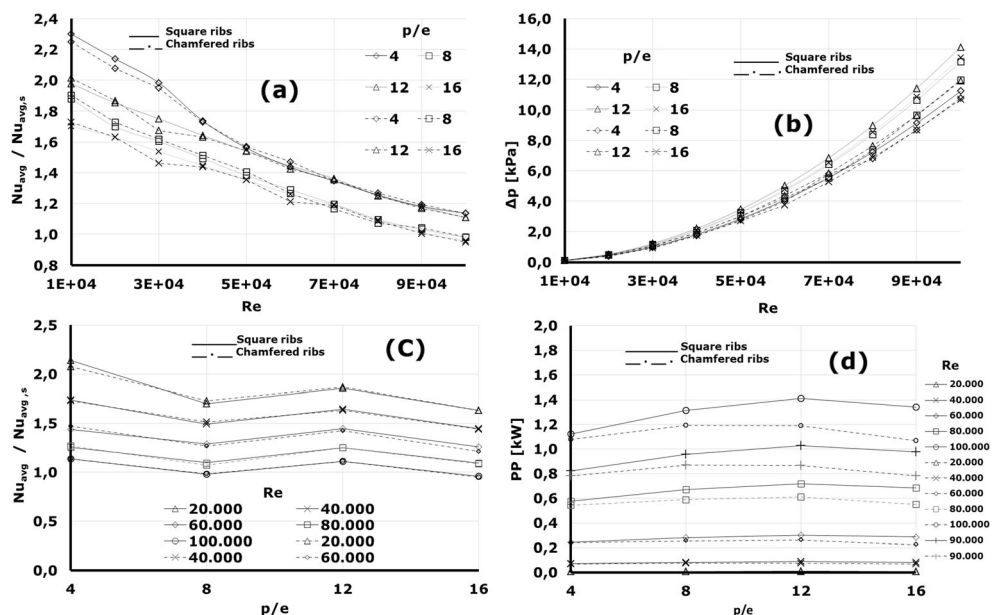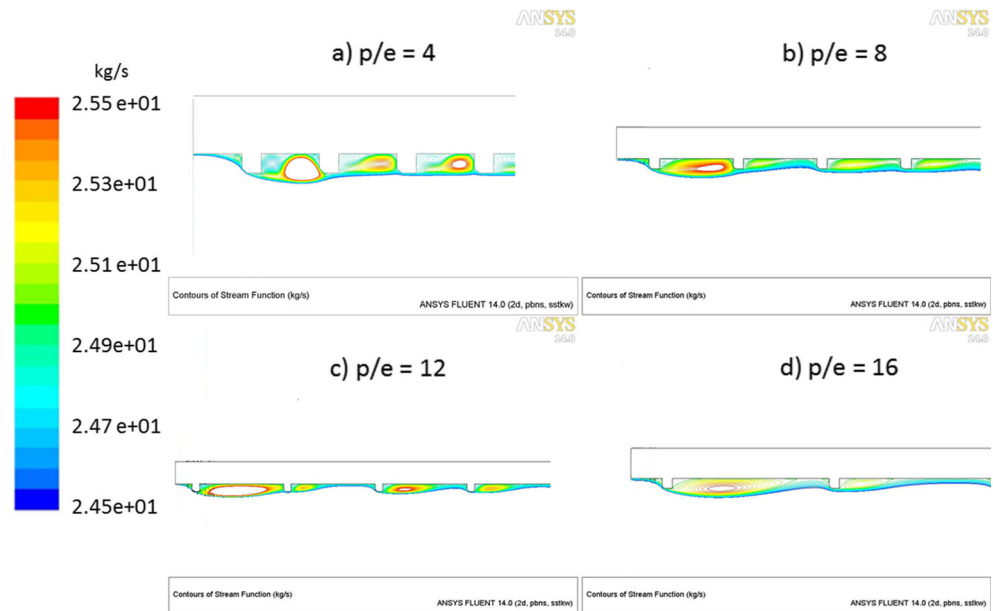
Fig. 7 Stream function at Re $=50\cdot10^3$ for the ribbed wall with chamfered edge ribs at different p/e, namely: (**a**) 4, (**b**) 8, (**c**) 12, (**d**) 16, nearby the inlet of the ribbed channel

– p/e = 12: creation of a vortex which does not occupy all the space between the ribs, therefore a free zone is left
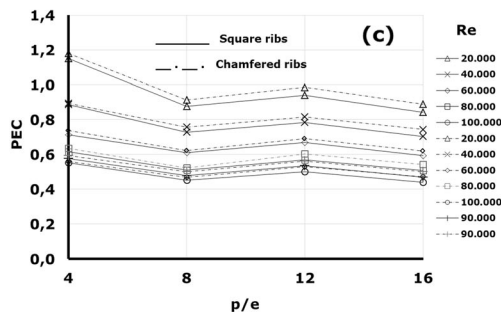

Fig. 8 Comparison between square and chamfered ribs: (**a**) friction factor ratio, (**b**) PEC index as function of Re, (**c**) PEC index as function of p/e

where fluid from the main stream is recalled. This provokes an improvement with respect to p/e = 8;

– p/e = 16: similar situation as p/e = 12, but the number of ribs is lower, therefore a deterioration of the heat exchange is detected.
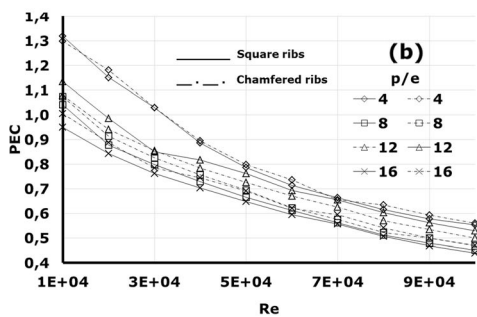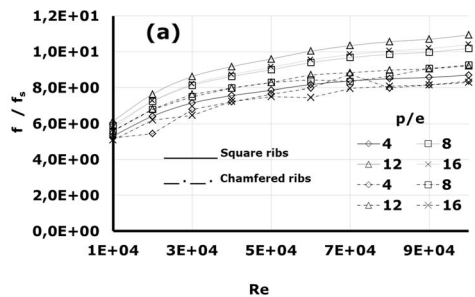
By analyzing the required PP, reported in Fig. 6(d), it can be detected that the ribs with the chamfered corner necessitate a lower pumping power, especially at high Re. Therefore, the chamfer results to be an effective solution to decrease pressure losses and the resulting PP.

At p/e = 12 the maximum pumping power is required, because the reattachment of the flow in the gap allows the interaction of the mainstream flow with the ribs, introducing concentrated losses. This situation does not happen or is very limited for p/e = 4 and 8, where the ribs do not act as concentrated losses. At p/e = 16, there is the interaction with the mainstream flow, but the number of ribs is lower (25% less), therefore the effect is limited.

Fig. 8(a) reports the friction-factor ratio profile. It is possible to observe that the case of square rib presents a regular trend, whereas in the cases with the chamfer absolute maximum with local peaks are visible, in particular for p/e = 4. This behavior is partially analyzed in Fig. 7 and it will be further clarified in the following with the aid of more streamlines fields.

Finally, Figs. 8(b) and 8(c) show the PEC index for the two different shapes of considered ribs. As already noted, the best performances are obtained at low Reynolds numbers and p/e equal to 4 and 8. At low Re, the ribs contribution to the thermal performance is relevant, instead at high-Re number the pressure drop increment is dominant. The PEC index decreases both with Reynolds and p/e increase.
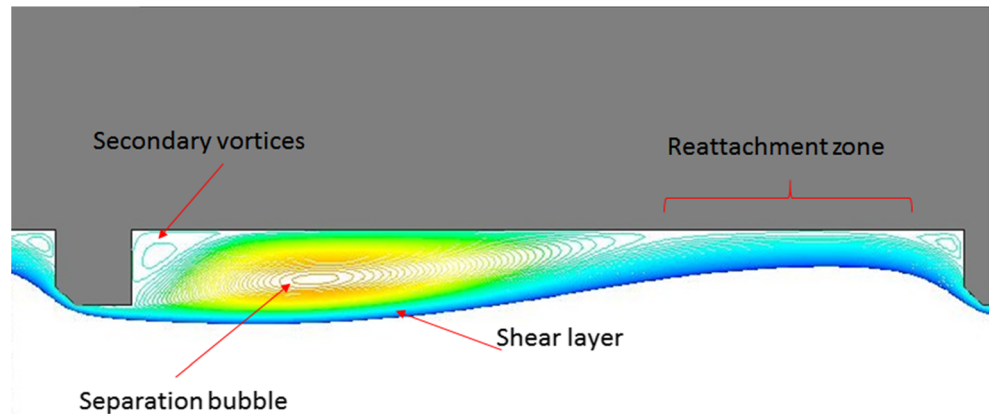
When ribbed surfaces are considered, a general improvement of thermal performances is detected, but due to the increased pressure drop, the global efficiency of the system does not improve for high Re and large p/e.

In general, from the analysis of Figs. 8(b) and 8(c), it is concluded that it is better to employ the ribs when Re results below $40 \cdot 10^3$ and the optimal dimensionless pitch could be chosen between 4 and 12, according to the admissible pressure losses with respect to the required thermal performance.

It should be also noted that Fig. 8(c) highlights the trend already detected in Fig. 6(c). This is determined by the same phenomenon, namely an alteration of the heat exchange due to the variation of the vortex structures originated between two consecutive ribs.

With the aim of analyzing in detail the fluid-dynamics behavior inside the ribbed pipe, contours of velocity, temperature

and stream-functions are shown for some of the analyzed cases, with particular reference to the anomalous trend reported in Fig. 8(a).

The physics of the fluid motion across the ribs could be considered as a case of the "Backward-facing step" (BFS) problem, widely analyzed in literature [19–22]. However, due to the presence of serial ribs, the reattachment length results not comparable with the previously analyzed BFS problems, and only a qualitative analysis of the shape of the vortexes is preliminary conducted.

The flow behind the backward-facing step is complex and involves various instability mechanisms. Some of the most common features behind the step recognized in the literature [19] are present in the current analysis.

The flow zone can be distinguished into three main regions namely, the shear layer region, separation bubble or

Fig. 10 Stream function at
$Re = 50 \cdot 10^3$ in the case of square
ribs for different p/e, namely: (a)
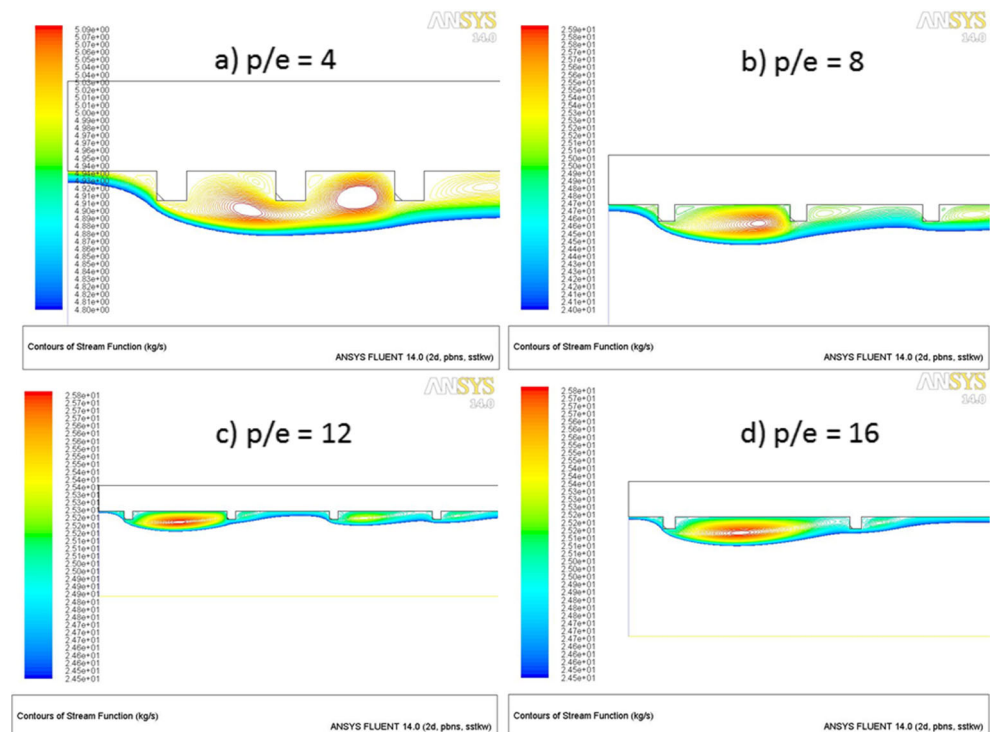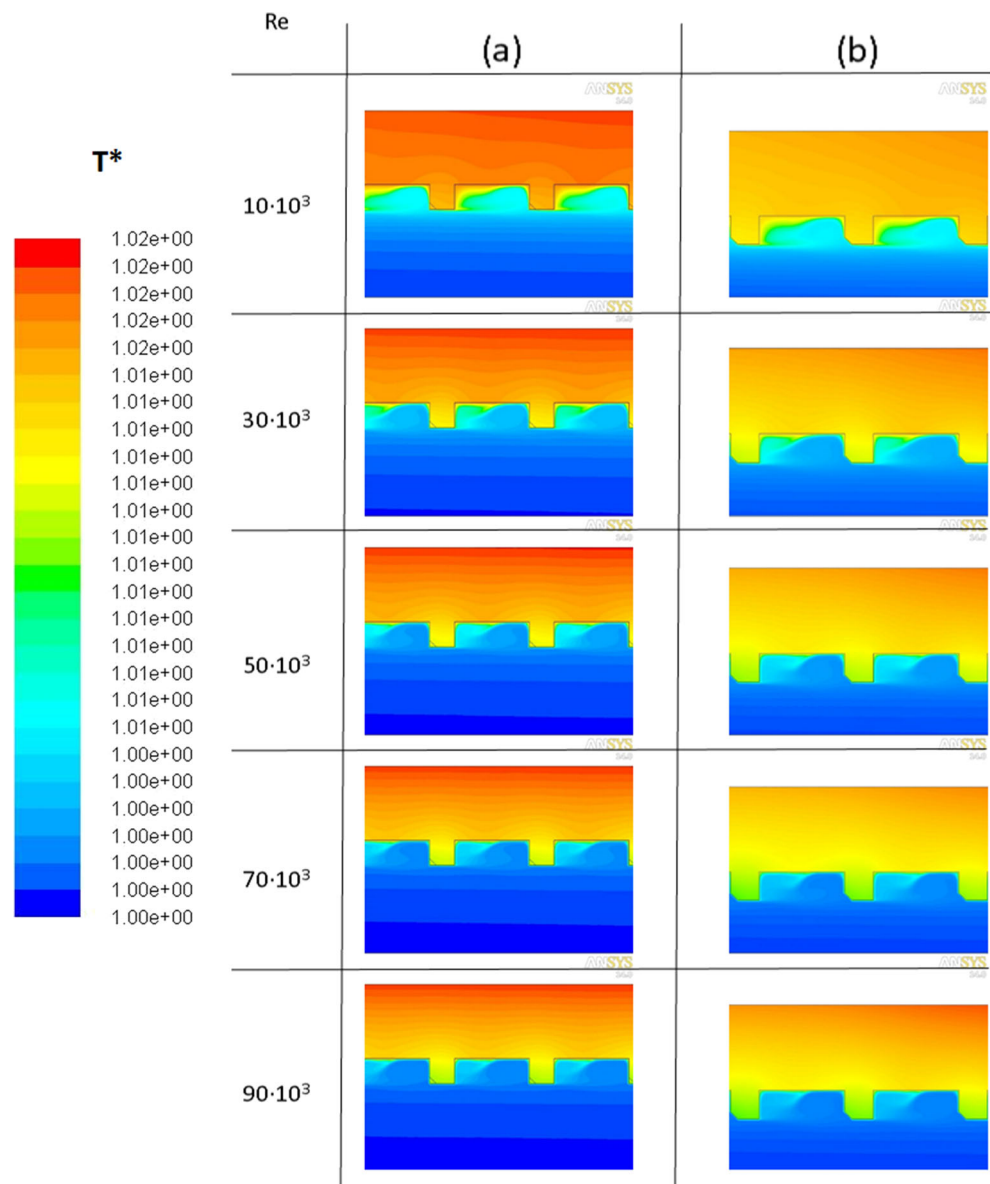4, (b) 8, (c) 12, (d) 16, nearby the
inlet of the ribbed channel

Fig. 11 Non dimensional temperature for square and chamfered ribs for different Re and p/e = 4

recirculation zone and the reattachment zone. The general characteristics of a BFS flow begins with an upstream boundary layer separating at the step edge due to the adverse pressure gradient that develops into a thin shear layer. As the flow progresses downstream, the shear layer grows in size with the amalgamation of the turbulent structures contained within.

In Fig. 9 the stream function across the ribs for the case with p/e = 12 and Re = 50·10³ is reported: the separation bubble of recirculation, the secondary vortices and an averaged shear layer, very smooth due to the steady solver and RANS turbulence model used, are clearly visible.

A reattachment zone, clearly influenced by the consecutive ribs presence and not comparable with BFS literature results, is also detected. Then, the fluid-dynamic behavior of the present case and the BFS is similar, but only the vortex-zone shape is comparable.

Figs. 7 and 10 show the stream function in the initial part of the ribbed channel for both chamfered edge and square ribs.

The bubble separation zone and the secondary vortex are present in all of the cases, but, by analyzing Fig. 7, it is clearly noticeable that for p/e = 4 the vortex structure does not have enough axial space for its development and, in particular between the first two ribs (Fig. 7a), the bubble of recirculation results very large.

Comparing the same case with square ribs (Fig. 10a), the recirculation zone result widely extended, with a double-eye recirculation bubble zone including the following rib. The nature of this double-eye bubble is due to the hard edge against which the flow slams, whereas in the case with chamfered edge rib, the initial distortion of the streamlines is much less pronounced.

At p/e = 8 (Figs. 7b and 10b), the bubble of recirculation fills completely the gap between the ribs and, by increasing the p/e value (Figs. 7(c-d) and 10(c-d)), the vortices structures are fully developed.

Fig. 11 reports dimensionless contours of Temperature, $T^* = T/T_{bulk}$, near the ribbed wall for p/e = 4, with (a) and without (b) chamfered ribs at different Reynolds number.

The contours of T^* show a negligible influence of the chamfer at low Reynolds number, with a wide diffusive thermal boundary layer and with a marked diffusive layer in correspondence of the secondary vortex zone. Instead, at high Reynolds number, heat transfer is dominated by the convective effect and the recirculation zone in the chamfered ribs case is wider with a lower mean temperature between the ribs and inside the solid ribs zone.

4 Conclusions

In this work a 2-D ribbed channel with square and chamfered ribs mounted on the principal walls and heated by a uniform heat flux is considered. Turbulators have e/d values equal to 0.05, whereas different pitches and Reynolds numbers are taken into account.

The fluid is water at ambient pressure and temperature. Simulations have shown that the introduction of the ribs augments both the heat transfer coefficients and the pressure drops. In the case of ribbed channel with chamfer there is a decrement of the pressure drop and consequently an increment of the PEC index. The highest Nusselt number values are detected for p/e equal to 4 and 12, both for square and chamfered shapes. In terms of heat transfer, the ribs presence is very influent at low Re number, while at high Re is more limited.

With reference to the required pumping power, maxima are obtained at p/e = 12 for the square case and at p/e = 8 for the chamfered case. The highest thermal performances are exhibited by the square turbulators, which provide also the highest losses. The Nusselt number rises as Reynolds numbers increase as well as the pumping power. The highest values of PEC index are detected at p/e = 4 and they increase as Re decreases.

References

1. Bianco V, Manca O, Nardini S (2014) Performance analysis of turbulent convection heat transfer of Al_2O_3water-nanofluid in circular tubes at constant wall temperature. Energy 77:403–413. doi:10.1016/j.energy.2014.09.025
2. Lee CK, Abdel-Moneim SA (2001) Computational analysis of heat transfer in turbulent flow past a horizontal surface with two-dimensional ribs. Int Commun Heat Mass Transfer 28(2):161–170. doi:10.1016/S0735-1933(01)00223-8
3. Tanda G (2004) Heat transfer in rectangular channels with transverse and V-shaped broken riebs. Int J Heat Mass Transfer 47(2):229–243. doi:10.1016/S0017-9310(03)00414-9
4. Promvonge P, Thianpong C (2008) Thermal performance assessment of turbulent channel flows over different shaped ribs. Int Commun Heat Mass Transfer 35(10):1327–1334. doi:10.1016/j.icheatmasstransfer.2008.07.016
5. Promvonge P, Chompookham T, Kwankaomeng S, Thianpong C (2010) Enhanced heat transfer in a triangular ribbed channel with longitudinal vortex generators. Energy Convers Manag 51(6):1242–1249. doi:10.1016/j.enconman.2009.12.035
6. Kim HM, Kim KY (2004) Design optimization of rib-roughened channel to enhance turbulent heat transfer. Int J Heat Mass Transf 47(23):5159–5168. doi:10.1016/j.ijheatmasstransfer.2004.05.035
7. Kim KM, Kim BS, Lee DH, Moon H, Cho HH (2010) Optimal design of transverse ribs in tubes for thermal performance enhancement. Energy 35(6):2400–2406. doi:10.1016/j.energy.2010.02.020
8. Xie G, Zheng S, Zhang W, Sundén B (2013) A numerical study of flow structure and heat transfer in a square channel with ribs combined downstream half-size or same-size ribs. Appl Therm Eng 61:289–300. doi:10.1016/j.applthermaleng.2013.07.054
9. Viswanathan AK, Tafti DK (2006) Detached eddy simulation of turbulent flow and heat transfer in a two-pass internal cooling duct. Int J Heat Fluid Flow 27(1):1–20. doi:10.1016/j.ijheatfluidflow.2005.07.002
10. Labbè O (2013) Large-eddy-simulation of flow and heat transfer in a ribbed duct. Comput Fluids 76:23–32. doi:10.1016/j.compfluid.2013.01.023
11. Dritselis CD (2014) Large eddy simulation of turbulent channel flow with transverse roughness elements on one wall. Int J Heat Fluid Flow 50:225–239. doi:10.1016/j.ijheatfluidflow.2014.08.008
12. Tan L, Zhang JZ, Xu HS (2014) Jet impingement on a rib-roughened wall inside semi-confined channel. Int J Therm Sci 86:210–218. doi:10.1016/j.ijthermalsci.2014.06.037
13. Caliskan S, Baskaya S (2012) Experimental investigation of impinging jet array heat transfer from a surface with V-shaped and convergent-divergent ribs. Int J Therm Sci 59:234–246. doi:10.1016/j.ijthermalsci.2012.04.013
14. Yadav AS, Bhagoria JL (2014) A numerical investigation of square sectioned transverse rib roughened solar air heater. Int J Therm Sci 79:111–131. doi:10.1016/j.ijthermalsci.2014.01.008
15. Manca O, Nardini S, Ricci D (2012) A numerical study of nanofluid forced convection in ribbed channels. Appl Therm Eng 37:280–292. doi:10.1016/j.applthermaleng.2011.11.030
16. Bejan A, Kraus AD (2003) Heat transfer Handbook. Wiley
17. Baehr HD, Stephan K (2011) Heat and mass transfer, 3rd edn. Springer
18. Incropera FD, DeWitt DP, Bergman TL, Lavine AS (2006) Fundamentals of heat and mass transfer, 6th edn. Wiley
19. Rajasekaran J (2011) On the flow characteristics behind a backward-facing step and the design of a new axisymmetric model for their study. Master Degree Thesis, University of Toronto
20. Rajasekaran J, Lavoie P (2011) Effect of boundary layer thickness on separated shear layer behind a backward-facing step. In: CASI Aero
21. Driver DM, Seegmiller HL, Marvin JG (1987) Time-dependent behavior of a reattaching shear layer. AIAA j 25(7):914–919
22. Kim JJ (1978) Investigation of separation and reattachment of a turbulent shear layer ow over a backward-facing step. PhD thesis, Stanford Universtiy
23. Menter FR (1994) Two equation eddy-viscosity turbulence models for engineering applications. AIAA J 32:1598–1605
24. Tennekes H, Lumley JL (1972) A first course in turbulence. The MIT Press
25. Wilcox DC (1994) Turbulence modeling for CFD. DCW Industries
26. Pope SB (2014) Turbulent flows. Cambridge University Press

27. ANSYS FLUENT Theory Guide (2001) ANSYS Inc., Release 14.0
28. Webb RL, Kim NH (2006) Principles of enhanced heat transfer, second edn. Taylor & Francis Group, New York
29. Karwa R, Solanki SC, Saini JS (2001) Thermo-hydraulic performance of solar air heaters having integral chamfered rib roughness on absorber plates. Energy 26(2):161–176
30. Layek A, Saini JS, Solanki SC (2009) Effect of chamfering on heat transfer and friction characteristics of solar air heater having absorber plate roughened with compound turbulators. Renew Energy 34(5):1292–1298. doi:10.1016/S0360-5442(00)00062-1
31. Schlichting H, Gersten K (2000) Boundary layer theory. Springer-Verlag, Berlin
32. Elsaadawy E, Mortazaci H, Hamed MS (2008) Turbulence modeling of forced convection heat transfer in two-dimensional ribbed channels. ASME J Electron Packag 130(3):0310111–03101117. doi:10.1115/1.2912182
33. Saberinejad H, Hashiehbaf A, Afrasiabian E (2010) A study of various numerical turbulence modeling methods in boundary layer excitation of a square Ribbed Channel. World Acad Sci Eng Technol 71:338–344
34. Haque A, Ahmad F, Yamada S, Raza S (2007) Assessment of Turbulence Models for Turbulent Flow over Backward Facing Step. In: Proceedings of the World Congress on Engineering. Vol IIWCE 2007, July 2–4, 2007, London, UK